Fracture investigation of refractories under combined mode I and mode II loading

Master Thesis at the Chair of Ceramics

Montanuniversität Leoben

Submitted by

Ru Zhou

Leoben, February 2017

AFFIDAVIT

I declare in lieu of oath, that I wrote this thesis and performed the associated research myself, using only literature cited in this volume.

This thesis is dedicated to my beloved parents.

Acknowledgements

First of all, I would like to acknowledge my supervisor Dr.mont Shengli Jin for his support and guidance throughout the duration of this work. Thank you for encourage and believe in me. Without his support it would not be possible to finish this thesis.

I would also like to express my sincere appreciation to my supervisor O.Univ.-Prof. Dipl.-Ing. Dr.mont. Harald Harmuth. Thank you for the enormous knowledge you brought me. His serious scientific attitude, rigorous scholarship spirit, and working style deeply affect and inspire me.

Besides my supervisor, I would like to appreciate Yajie Dai for helping me about the DIC work. I thank for her kindness and help.

Furthermore, I am indebted to my colleagues from Chair of Ceramics and it was a great honor to work with them. Particularly, I would like to thank the assistance from Mr. Robert Caks, Mr. Robert Obenaus-Emler and Mr. Alexander Halacek.

A special gratitude is given to my parents for their supporting, patience and understanding.

Abstract

This research aims to investigate the fracture behavior of two refractory materials under combined mode I and mode II conditions by a special wedge splitting test arrangement according to Tschegg [1].

By the wedge splitting test, the nominal notch tensile strength and specific fracture energy were studied for two materials, a magnesia material and a magnesia spinel material. In comparison with the pure magnesia material, magnesia spinel material has a lower nominal notch tensile strength and higher specific fracture energy. The wedge angle has influences on the determination of mechanical properties of both materials: The specific fracture energy of the magnesia spinel material does not show monotonous tendency with increasing asymmetrical wedge, and their nominal notch tensile strengths decrease with respect to asymmetrical wedge angle. In contrast, the specific fracture energy of the pure magnesia material increases with increasing asymmetrical wedge angle. Their nominal notch tensile strengths increase with the asymmetrical wedge angle and reach a plateau in 15-22.5°. Moreover, the fracture parameters measured under the asymmetrical loading with the wedge angle 10° are slightly lower than those under the symmetrical loading with the wedge angle 10°.

Based on DIC strain measurement, the initiation and the propagation of the cracks and the development of fracture process zone were analyzed. Compared to the pure magnesia material, the magnesia spinel material develops a higher amount of microcracks, causing a larger fracture process zone. The fracture process zone in the magnesia spinel material develops before reaching the maximum load, and during the crack propagation process, crack branching phenomenon can be observed. Besides, the asymmetrical loading condition gives rise to a narrow crack propagation zone. In the case of pure magnesia material, the fracture process zone develops after reaching the maximum load and no crack branching phenomenon takes place; only a main macro-crack can be observed. For both materials, higher asymmetrical wedge angles result in more instable macro-crack growth.

Table of contents

PROBLEM DEFINITION

Refractory materials are applied in high temperature industries for producing cement, steel, glass and nonferrous metals etc. They experience serious working conditions, for instances, slag corrosion and erosion, thermal cycling and mechanical/thermo-mechanical loadings. From mechanical point of view, fracture could occur due to the thermal shock during operations. Determination of thermal shock resistance is one important factor to assess the performance of refractories under thermomechanical loads.

Wedge splitting test (WST) according to Tschegg [2] has been applied successfully for decades, to characterize the failure of refractories under mode I. Out of this test the specific fracture energy can be calculated and used for further calculation of characteristic length or brittleness number, which quantitatively define the thermal shock resistance of refractories. The normal procedure applies a wedge shape that loads the specimen mainly by horizontal forces according to mode I. So far the influence of shear forces, i.e. a simultaneous mode II loading, on the determination of fracture parameters of refractories is rarely investigated. To increase the understanding, asymmetrical loading during the wedge splitting test will be performed using an asymmetrically acting wedge according to a further patent of Tschegg [1].The thesis aims to investigate the influences of asymmetrical wedge angle on the fracture parameters determination and crack propagation of refractories.

CHAPTER 1: STATE OF THE ART

1.1 Introduction

The fracture of refractories under mode I involves crack initiation and propagation. During the crack propagation, fracture process zone forms. Wedge splitting test according to Tschegg [2] enables stable crack propagation in the refractories. Digital image correlation (DIC) technique is often used to visualize the strain field in the materials under loading. In this chapter, the state of art of mode I fracture mechanics of refractory materials, the wedge splitting test and the digital image correlation technique were briefly reviewed.

1.2 Fracture of ordinary ceramic refractory materials

1.2.1 Linear elastic fracture mechanics (LEFM)

Linear elastic fracture mechanics has been developed to describe crack growth and fracture within a material under essentially linear elastic conditions. It is based on the assumptions that the material expansions are proportional to tensions and the energy consumption is only used for creating the fracture area [3]. In general there are three modes for the opening of crack in fracture mechanics: Mode I, Mode II and Model III (shown in Fig.1). Mode I is the tensile opening mode, in which the crack faces separate in a direction normal to the plane of the crack. Mode II is the in-plane sliding or shear mode, in which the crack faces are mutually sheared in the direction normal to the crack front. Mode III is the tearing or out of plane mode, in which the crack faces are sheared parallel to the crack front [3].
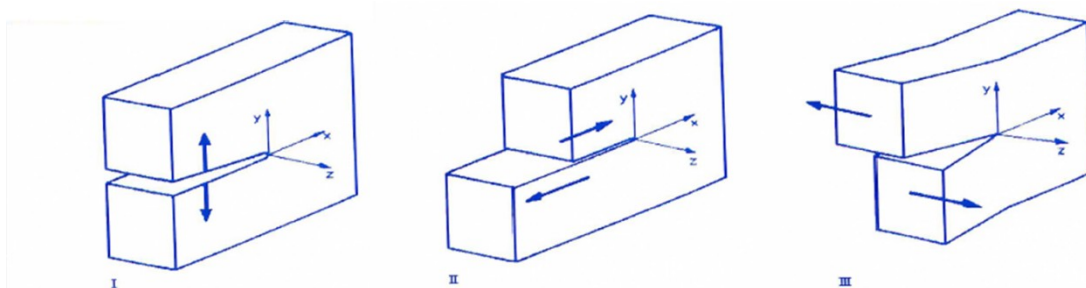
Fig.1: Three basic modes of crack propagation [3]

In LEFM, the energy criterion according to Griffith [4] and the stress intensity according to Irwin [5] are very essential. For the infinite large plane, the general equations of strain energy release rate G and stress intensity factor K_I are shown in Eq. (1) and Eq. (2):

$$G = \frac{\sigma^2\, Y\, \pi\, a}{E} \tag{1}$$

where G is the strain energy release rate, σ is the tensile stress, a is the crack length, Y is the geometry factor and E is the Young's modulus. The strain energy release rate is the rate at which energy is absorbed by growth of the crack.

$$K_I = \sigma\, Y\, \sqrt{\pi\, a} \tag{2}$$

where K_I is the stress intensity factor.

When the crack propagation takes place in the critical case, the equations of the critical intensity factor K_{IC} and the critical strain energy release rate G_c can be described as:

$$G_c = \frac{\sigma_f^2\, Y\, \pi\, a}{E} \tag{3}$$

$$K_{Ic} = \sigma_f\, Y\, \sqrt{\pi\, a} \tag{4}$$

$$\sigma_f = \sqrt{\frac{2E\gamma_0}{\pi a}} \tag{5}$$

here σ_f is tensile strength and γ_0 is surface energy. The critical intensity factor K_{IC} can be designated as fracture toughness during the crack propagation. The fracture toughness is a property which describes the ability of a material containing a crack to resist fracture. It is a material constant and an important fracture mechanical evaluation criterion for materials in LEFM conditions.

Combining the Eq. (4) and Eq. (5), the following relation between fracture toughness and surface energy is received.

$$K_{Ic} = Y\sqrt{2E\gamma_0} \tag{6}$$

Normally the fracture toughness values of refractory materials are rather low, because the strengths of refractories are not very high and their intrinsic flaws are very large.

The range of the fracture toughness of refractories is about 0.2 to 1.5 MPa $\cdot$ m$^{1/2}$.

In general the fracture behavior of refractories is very complicated. The linear fracture mechanics available today is not sufficient to describe such a complicated fracture behavior of refractories [6]. But the linear elastic fracture mechanics (LEFM) is still very important for understanding non-linear phenomena.

1.2.2 Deviations from pure linear elastic fracture mechanics

The deviations from pure linear elastic fracture is the result of inelastic phenomena taking place in crack front process zone ahead of the main crack and the region behind the crack front across the newly formed fracture surfaces. The deviations from elastic fracture behavior are: the irreversible deformation is around the crack tip of the fracture surface (micro process zone), the crack surface is not planar, and crack branching may occur and the grain bridges behind the crack tip consume energy by friction [3].

To address the nonlinear inelastic phenomena, Rice formulated the J-integral and presented as [7]:

$$J = \int_{\Gamma} \left(w \, dy - T_i \, \frac{\partial u_i}{\partial x} \, ds \right) \tag{7}$$

where w is the elastic strain energy density; Γ is the arbitrary path clockwise around the apex of the crack; T_i is the traction vector; u_i is the displacement vector; ds is the increment length along the path Γ. If Γ is a closed curve around the crack tip, the J-integral is independent of the integration path Γ. From the value J a fracture criterion J_c can be deduced. In the linear elastic case, the value of J is equal to the crack propagation force according to Irwin [5],

$$J_c = 2\gamma_0 \tag{8}$$

The value $2\gamma_0$ is also called critical Irwin's crack propagation force.

During the crack propagation of materials, if the process zone size is not negligible compared with the size of specimens, macroscopic fracture behavior becomes non-linear, and displays R-curve behavior. It was proved that R-curve behavior exists in most polycrystalline ceramics with large grain size refractories and ceramics composites [8-11]. A schematically rising R-curve behavior is illustrated in Fig.2. The crack growth resistance K_R is an important quantity and is equal to the change of the potential energy with the crack surface area A.

The R-curve rises with crack extension (Δa) due to the residual strain energy effect and grain bridging effect in the process zone wake as well as the grain bridging and interlocking tractions developed along the fracture surfaces behind the propagating crack tip [9,10]. The relationship between the process zone and the following process zone wake region is shown in Fig.3. There are many microcracks and phase transformation constituting the irreversible deformation processes in the process zone wake. The residual strain energy effect is presumed that compressive stresses derived from the irreversible deformation processes shield the crack tip stresses from external stresses. The grain bridging effect is that the grain–bridging tractions between fracture surfaces reduce crack tip stresses. These two effects can lead to the increase of the fracture toughness values of refractories.
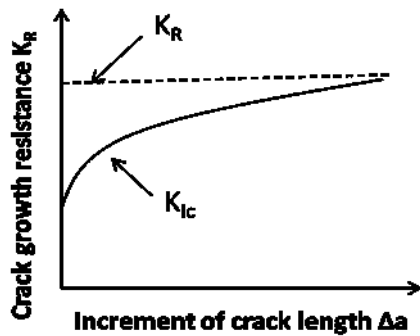
Fig.2: Rising R-curve behavior
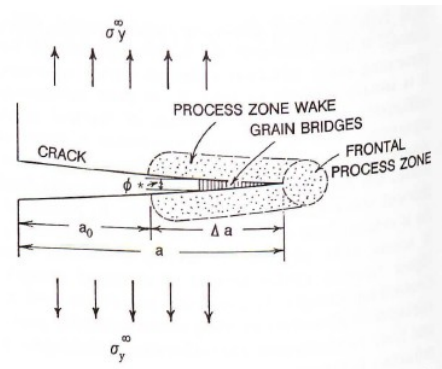
Fig.3: Schematical drawing of a process zone, process zone wake and grain bridging zone [6]

Bradt [12] has proved that the energy–absorbing phenomena occur in the vicinity of the cracks of refractories and these consume a large amount of energy as the crack front advances. These events take place in two different regions: the process zone in front of the advancing crack and the following wake region. These two different regions are so called fracture process zone. Fig.4 schematically illustrates the total process zone. In the front of the crack, microcracking is prevalent and there is usually considerable crack branching. In the process wake, the refractory microstructural elements such as aggregates are able to interact across the newly formed crack surface.
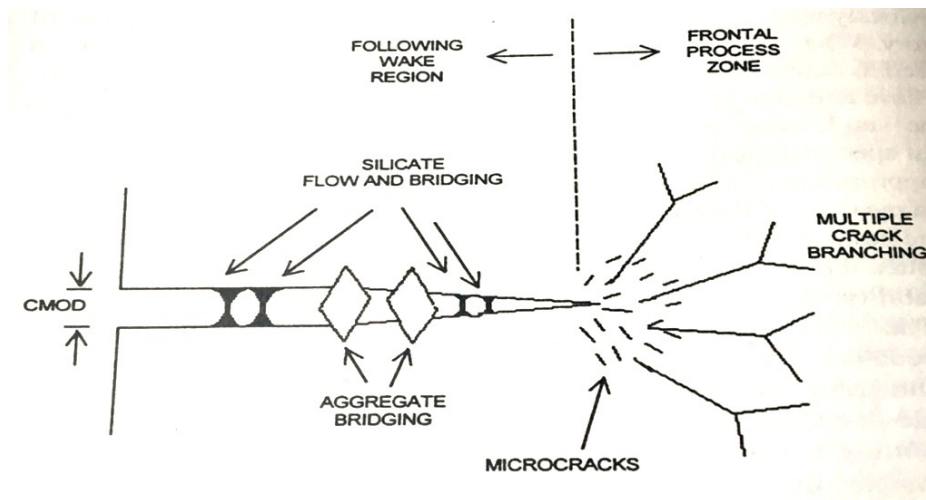
Fig.4: Fracture process zone of refractories [12]

Once a crack begins to propagate, it develops a steady-state frontal process zone. The size of this frontal process region varies from different refractory materials. But it can be simply estimated by using a Dugdale-like approach. In Dugdale model (shown in Fig.5a), it is assumed that there is a plastic zone near the crack tip [13]. Within the plastic zone, the stress equal to yield stress acts across the crack. The Barenblatt model is similar, but he assumed the stresses vary with the deformation [14]. Based on the Dugdale model and Barenblatt model, Hillerborg [15] introduced a fictitious crack model (shown in Fig.5b) which is the nonlinear fracture mechanical model and considered the energy consumption in fracture process zone.

a)   b)
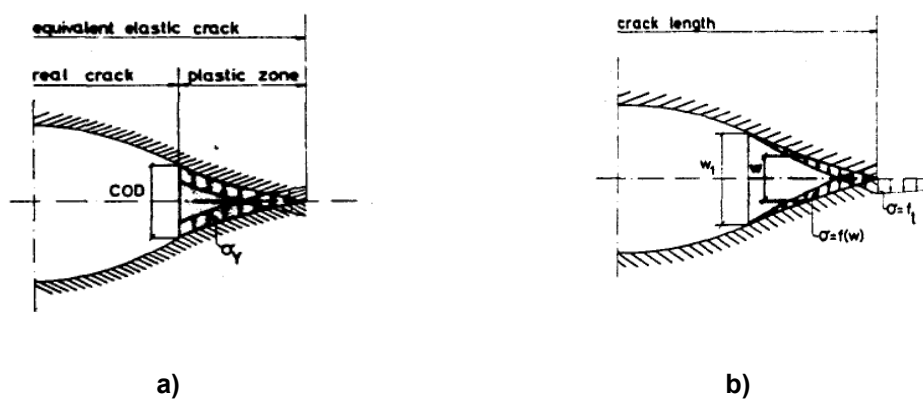
Fig.5: a) The Dugdale model for crack tip plasticity and b) The Hillerborg model [15]

The fictitious crack model is described only for Mode I (the opening mode). It is a general mode which in principle is valid for all kinds of materials [16]. In the fictitious crack model, the crack is assumed to propagate when the stress at the crack tip

reaches the tensile strength f_t. The stress is not assumed to fall to zero at once when the crack opens, but it decreases with increasing crack width until an ultimate crack opening of u_{ult} is achieved (Fig.6). The relation representing the decrease in stress with increasing strain is called the strain softening behavior.
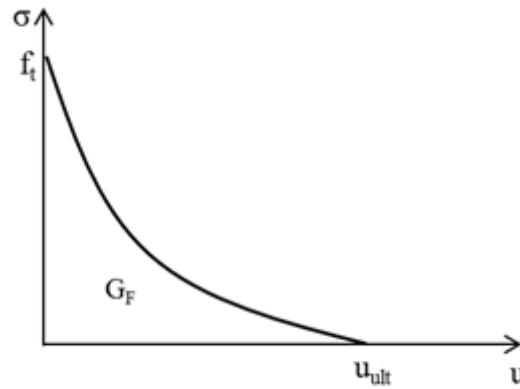
Fig.6: The stress-softening behavior

The area under the stress-softening curve is the total specific fracture energy G_F, the equation of specific fracture energy can be described as:

$$G_F = \int_0^{u_{ult}} \sigma(u)\, du \qquad\qquad (9)$$

Where $\sigma(u)$ is the function of stress to the crack face distance.

The fictitious crack model is a representative of cohesive crack models for quasi-brittle materials. Normally, the fracture of quasi-brittle materials such as rocks, concretes, and refractories can be characterized by the strain-softening curve, the tensile strength f_t and the total specific fracture energy G_F. The total specific fracture energy can be determined by the wedge splitting test which is introduced in the next section.

In a word, the development of the fracture process zone has a significant influence on the fracture behavior which is important for the industrial application of quasi-brittle materials and safety design. The size of the fracture process zone is dependent on the specimen shape, including the specimen ligament length and width, the type of loading and material properties.

1.2.3 Thermal stress induced fracture

When fracture takes place as a consequence of thermal stresses generated

7

during the thermal cycling or rapid environmental temperature variation, the extent of damage during fracture is controlled by an energy criterion. It was explained by Hasselman [17, 18]. He derived and defined the kinetic thermal shock damage resistance parameter R'''' for kinetic crack growth, it is represented as:

$$R''''= E\gamma_{wof}/\sigma_f^2 \tag{10}$$

where E is the elastic modulus and γ_{wof} is the work-of-fracture as mentioned in the publications of Nakayama [19] and Tattersall and Tappin [20] and etc.

The work-of- fracture equation is [19]:

$$\gamma_{wof} = \int \frac{Pdu}{2A} \tag{11}$$

where the $\int Pdu$ is the area under the load-displacement curve and A is the cross sectional area of the remaining ligament of specimen after notching. The factor of 2 is included because when a specimen is fractured, then two newly created fracture surfaces form.

Hasselman defines a quasi-static crack growth damage resistance parameter R_{st} in a similar way of Eq. (10) which can be expressed as [18]:

$$R_{st} = (\gamma_{wof}/E\alpha^2)^{1/2} \tag{12}$$

where α is the coefficient of thermal expansion and the other parameters are as previously described.

When the thermoelastic stress is represented in a simple form for linear elastic in one dimension, it can be expressed as:

$$\sigma = \alpha E f(T) \tag{13}$$

here $f(T)$ is a temperature function, it further shows:

$$\sigma^2 \sim \alpha^2 E^2 \tag{14}$$

Combining the Eq. (12) with (10) for $E\alpha^2$ reveals that both R'''' and R_{st} are inversely related to the strength squared divided by the elastic modulus. This quantity (σ^2/E) is proportional to the stored elastic strain energy which is the driving force for fracture or crack extension.

It is shown that thermal stress damage resistance decreases as the strength increases from the above explanation. Usually, high strength refractory materials are much more susceptible to thermal shock damage.

1.3 Wedge splitting test

The determination of the specific fracture energy G_F and the strain softening diagram are necessary. The most direct way to determine these material properties would be uniaxial tensile tests. However, it is difficult to carry out such uniaxial tensile tests, because of the insufficient stiffness of testing device and difficult preparation of specimens. Therefore, this test is not suitable as a standard test for refractories. It is easier to perform stable tests on notched specimens subjected to bending. However, three point bending test (TPBT) and compact tension test (CT-test) have drawbacks with regard to future used as standard tests [21]. The wedge splitting test (WST) is an alternative method to perform stable fracture mechanics test on quasi-brittle materials which enables stable fracture and can produce reliable data [22]. Consequently, the wedge splitting test is widely used in quasi-brittle materials. Some applications of WST, especially the application of refractories, are briefly presented in the next part.

1.3.1 Applications of wedge splitting test

The wedge splitting test was proposed by Linsbauer and Tschegg [23] to determine the fracture parameters of concrete and later was also applied by Bruehwiler and Wittmann [21].

The applicability of the wedge splitting test for determining fracture properties of fiber-reinforced concrete was discussed by Löfgren [24]. Different specimen geometries were used in the investigation (shown in Fig.7). To avoid any wall effects, the specimens were sawed to obtain notches and then casted with two different depths of 150 mm and 200 mm, the thickness of all specimens was 100 mm. The specimens were water cured until testing. The tests were carried out in a deformation controlled testing machine (screw driven), see Fig.8. The rate of the vertical displacement was approximately 0.15 mm/min, which resulted in a CMOD-rate of 0.08 mm/min. The crack mouth opening (CMOD) was measured with a clip gauge, placed in the groove (as indicated in Fig.7), the horizontal deformation at the center of the roller bearings was measured with two LVDT-gauges and the vertical deformation was measured with a LVDT-gauge. In the tests, a wedge angle of 15° was used and the roller bearing used for tests was double row deep groove.
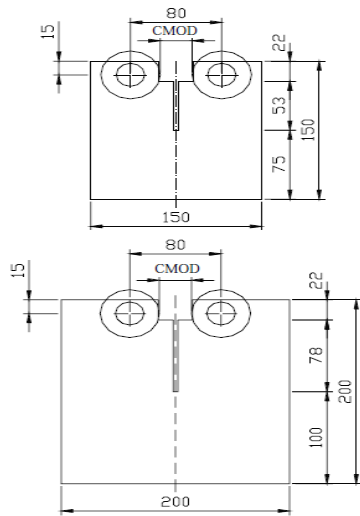
Fig.7: Geometries of specimens [24]   **Fig.8: Test set up [24]**
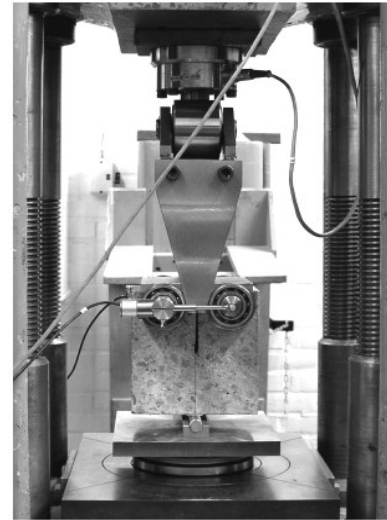
S. E. Stanzl-Tschegg et al investigated the wood fracture characterization utilizing WST [25]. In this study, the fracture energy of spruce wood was determined in the TL and RL direction (illustrated in Fig.9). The testing method according to Tschegg [2] and a cubic specimen with a groove and a starter notch are shown in Fig.10. The loading facility was placed on the groove. It consisted of two load transmission pieces and a slender wedge with an angle of 5-10°. The loads were transmitted from wedge to specimen via roll bodies (see Fig.10b) so as to reduce the friction. Therefore, the energy losses due to friction can be reduced to a negligible amount (smaller than 1%). During the test, a wedge angle of 10° was chosen and the force F_V from the testing machine was measured. The displacement gages were mounted on both ends of grooves in the line of horizontal force acting, so that the crack mouth opening displacement was measured.
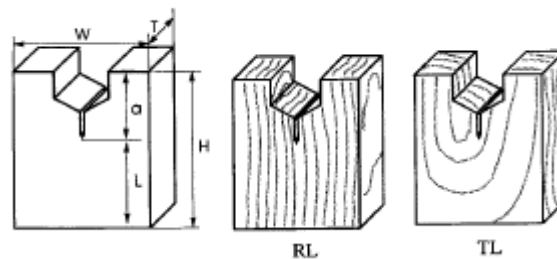
Fig.9: Characterization of specimen orientations for WST [25]
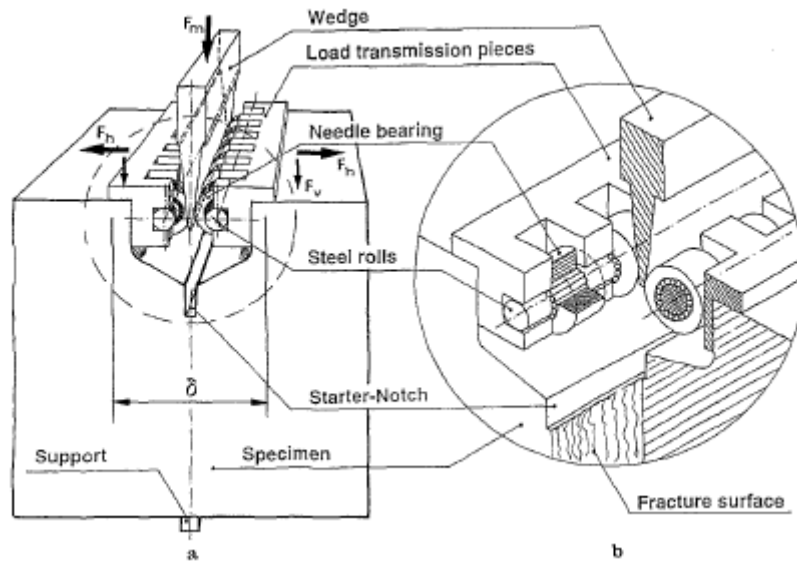
Fig.10: a) Cubic specimen with loading facility b) Load transmission [25]

1.3.2 Wedge splitting test of refractories

It is applicable for the determination of the specific fracture energy of refractories by using the WST according to Tschegg [2, 26] because of the stable crack propagation in specimens with a higher ratio of fracture surface area to specimen volume [27]. The detailed description of wedge splitting test and applications I have mentioned above [21, 23-25]. In this section, only the load-displacement curve obtained from the wedge splitting test (see Fig.11) and the further calculations about the fracture energy, nominal notch tensile strength are described.

The vertical force (F_V) was measured by a load cell. The horizontal force (F_H) was calculated from F_V by using Eq. (15) [2]:

$$F_H = \frac{F_V}{2 \tan(\beta/2)} \tag{15}$$

Here β is the wedge angle. The wedge splitting test was a displacement controlled test and was performed with a loading velocity of 0.5 mm/min in the vertical direction. The horizontal displacement was measured by video extensometers. After test, a load-displacement curve can be gained automatically and the fracture mechanical parameters of refractories can be determined from test results.

In many cases the test could be performed until the descending load approaches to zero, so that the total specific fracture energy can be gained. However, in the case

of refractory materials with largely reduced brittleness, the wedge may eventually hit the groove of the specimen before the load approaches to zero. Hence, only a major part of the specific fracture energy (G_f') can be calculated by integration [2]:

$$G_f{}' = \frac{1}{A} \int_0^\delta F_H \cdot d\delta_H \qquad (16)$$

Here δ_H is the horizontal displacement, A is the projected area and δ is the horizontal displacement at 15% of the maximum load.

The nominal notch tensile strength σ_{NT} can be calculated from the maximum horizontal load $F_{H,max}$ using Eq. (17) [2]:

$$\sigma_{NT} = \frac{F_{H,max}}{bh}\left(1 + \frac{6y}{h}\right) \qquad (17)$$

where h and b are the height and the width of the fracture surface area, respectively, and y is the vertical distance of the centre of gravity of fracture surface from the horizontal force. The nominal notch tensile strength comprises the contribution of tensile stress and flexural stress.
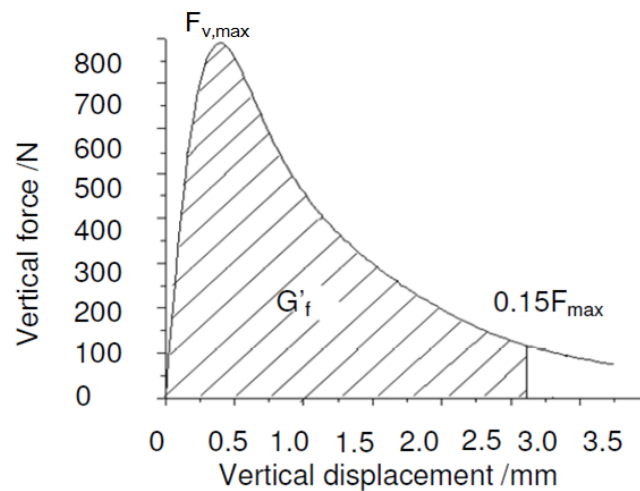
Fig.11: A typical load-displacement curve of WST [28]

1.4 Digital image correlation (DIC)

1.4.1 Digital image correlation technique (DIC)

Digital image correlation (DIC) is an optical method that employs tracking and image registration techniques for accurate 2D and 3D measurements of changes in images [29-31]. This is often used to measure deformation, displacement, strain,

and optical flow, and it is widely applied in many areas of science and engineering. This non-contacting optical method compares the images of the specimen surfaces obtained before and during deformation. It highlights the phenomenon of crack branching which corresponds to micro-cracks during the crack propagation. As DIC is a non-contacting and non-destructive method, it does not affect the development of the fracture process zone. Therefore, DIC is widely used to study fracture processes of quasi-brittle materials.

Digital image correlation consists in two digital images corresponding to two different mechanical states, a reference state and a deformed state. Each pixel of these images stores a grey level value due to a pattern at the surface of the material that is called speckle pattern [32]. The measurement of displacement field between these two different mechanical states is based on a virtual grid defined in the reference image. The displacement of each point of this grid is calculated on a subset surrounding the considered point in these two different mechanical states by comparing the grey level distribution of pixels. A relatively large area surrounding subset is so called the region of interest (ROI) which is shown in Fig.12 [33].
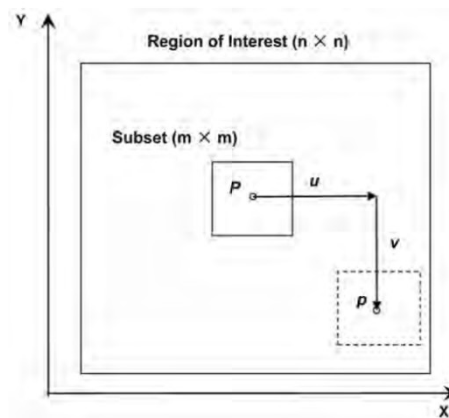
Fig.12: Displacement (u and v) of a subset in ROI [33]

The purpose of DIC is to correlate the original and displaced subsets via the best matching of the intensity patterns. If the intensity patterns of two subsets in reference and deformed images are best matched, the two subsets are considered the same.

The intensity values that located at position P can be expressed as [33]:

$$I(P) = I(X, Y) \tag{18}$$

After deformation, point P is displaced to position p and the intensity values are changed to [32]:

$$I'(p) = I'(X + u, Y + v) \tag{19}$$

In order to find a best match of the two subsets, cross- correlation with a fast Fourier transform method is used to search the intensity values in the ROI. The cross-correlation function R is defined as the two dimensional spatial convolution of I' with the separation vector s in the correlation plane:

$$R(s) = \int I_1(P)I'(P + s)dP \tag{20}$$

There is a sharp peak of the cross-correlation function appearing on the correlation plane. Giving a subset of a pattern involving several speckles, the peak of cross-correlation $R(s)$ will reach a maximum in the ROI as $\vec{s} = \vec{u}$. The highest peak exhibits that it is the most probable match of the subset between reference and current images. The principle of DIC determines the average displacement of a small group of a speckle that forms a unique speckle pattern within the subset rather than determines the displacement of an individual speckle [34]. The DIC processing divides a digital image into subsets and then the cross correlation is calculated over all subsets. Thus, one displacement can be obtained for each subset. A full-field displacement within the image can be determined through assembly of displacement vectors.

1.4.2 Application of digital image correlation for refractories

Robert et al. [35] investigated the mechanical behavior of a fiber reinforced refractory castable by utilizing a 3-D digital image correlation technique. Under tension or bending condition, refractory castables exhibit very low fracture strain levels [36-39]. The 3-D digital image correlation (3-D DIC) allows such low strain levels to be measured. It is possible to reach similar strain resolution levels and to avoid the problem of position dependence related to the heterogeneous nature of the strain and to strain localization phenomena by 3-D image correlation. The stereo rig was composed of two 8-bit Qimaging$^{®}$ Qicam digital cameras with a CCD resolution of 1360×1036 pixels^2. They used Computar 25 mm f1.3 and Nikkor Nikon 60 mm f2.8 macro lenses in the experiments. Typical magnification factors g were g_b = 10.3 pixels/mm for bending tests (Computar lenses) and g_t = 28 pixels/ mm for tensile tests (Nikkor lenses). For the 4-point bending test the dimensions of specimens were $25 \times 25 \times 150$ mm^3 with a region of interest (ROI) of 25×125 mm^2 (in dashed lines in Fig. 13–left). Dimensions of the specimens for tensile test were $25 \times 30 \times 30$ mm^3 in the

reduced section with a ROI of 25 × 46 mm^2 (in dashed lines in Fig.13-right). Typical step sizes were 5 pixels for the bending test images and 10 pixels for the tensile test images. DIC was performed using Vic-2D$^®$ software [40] between reference and deformed images when varying the subset size from 9 to 61 pixels (9, 11, 15, 21, 25, 31, 41 and 61).
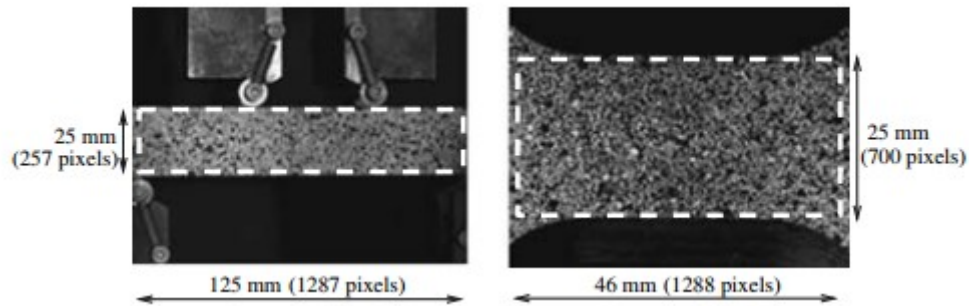
Fig.13: Region of interest (ROI) in dashed line for the bending test specimen (left) and for the tensile test specimen (right) [35]

Orteu et al. [41] have applied the 3-D DIC technique to characterize the behavior of ceramic refractories reinforced with metallic fibers. As cementitious materials, ceramic refractories are characterized by a quasi-brittle macro-mechanical behavior [42, 43]. Incorporation of metallic fibers can significantly improve their mechanical performances in terms of toughness, strain capacity or energy absorption capacity. In such composites, fibers act as bridging ligaments behind the crack tip resisting crack propagation. Furthermore, most reinforced concretes use short fibers with a quasi-random distribution in the composite in practice. Binocular stereovision is a technique for recovering the 3D structure of a scene from two different viewpoints (see Fig.14) where P(X,Y,Z) is the 3D point to be measured, $P_1(u_1,v_1)$ and $P_2(u_2,v_2)$ are its stereo-projections in the images, C_1 and C_2 are the optical centers of the two cameras (Fig.15). From a pair of images, it is possible to compute the 3D coordinates of a physical 3D point by triangulation. The 3D optical methods have been used to provide the validation step in the development of links between the micro-mechanical and the macro-mechanical scales and measure displacement/strain fields during macroscopic tensile tests on notched samples. In this study, tests were performed with an MTS 810 servo-hydraulic universal testing machine. Specimens were glued on rigid water cooled metallic plates. The temperature during the tests was from 20 to 500℃. The sample size was of 150×25×25 mm^3. In order to localize the crack initiation site in the

extensometer gauge lengths and to allow accurate crack-opening measurements, a 2-mm-wide and 2-mm-deep notch was manufactured at the sample periphery.
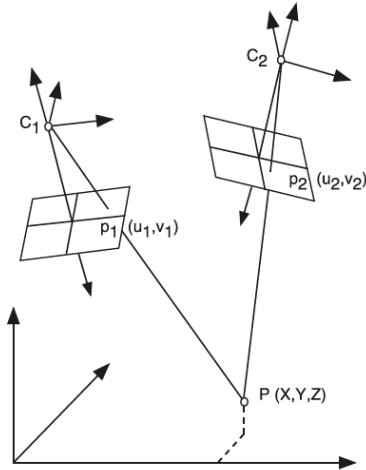
Fig.14: Binocular stereovision [41]   **Fig.15: The stereo rig used in experiments [41]**

Belrhiti et al. [44] investigated the impact of micro-cracks on fracture behavior of magnesia products using wedge splitting test and digital image correlation. In this study, an 8-bits CMOS camera (1600 × 1900 pixels^2) used to record images was placed in front of the speckled surface to perform optical measurements (see Fig.16). This allows studying crack growth during mechanical tests and the strain state around the crack tip. The acquisition frequency was 1 image/s. According to DIC principle, this area was subdivided using subsets of 32 × 32 pixels^2 with a gap of 8 × 8 pixels^2 and a scale factor of 0.067 mm/pixels.
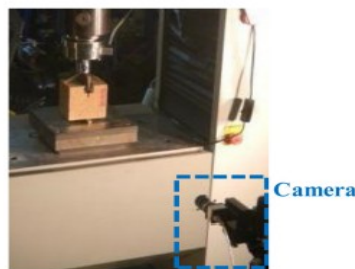
Fig.16: The set-up of experiments [44]

The compressive closure of dry joints in two classes of refractory bricks (magnesia carbon and magnesia chromite bricks) was investigated by Andreev et al. [45]. The measurements of bricks were performed in wide temperature range. The

process of joint closure was measured indirectly by compressing samples with and without joints. The samples for tests were cut from industrial bricks to dimensions of $100 \times 50 \times 50$ mm^3 and the faces were not polished. Digital Image Correlation (DIC) was used to measure the displacements of the bricks and the dry joint. Here a CCD camera (Fig.17), with a resolution of 1380×1024 pixels, was applied to take pictures. A grey scale random pattern was needed on the surface of the specimen; with which DIC technique can work well. In this work, the natural pattern of the bricks was enough to produce a suitable pattern. By recognizing this pattern mathematically, the intensity of each pixel in the reference and deformed images can be traced and the displacement vector can be determined.
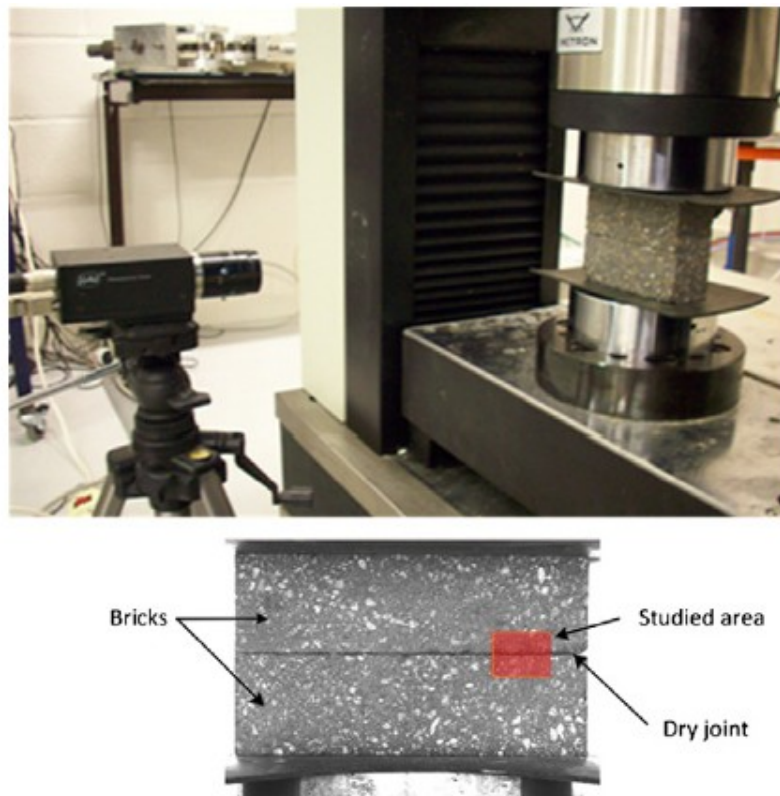
Fig.17: The set-up of experiments [45]

CHAPTER 2: FRACTURE OF MAGNESIA AND MEGNESIA SPINEL REFRACTORIES UNDER SYMMETRICAL AND ASYMMETRICAL LOADING

2.1 Introduction

In the literature mainly symmetrical loading applying for wedge splitting test of refractories were described. Until now, no studies relating asymmetrical loading on the refractories in terms of the wedge splitting test are available. In this chapter a testing setup was designed for applying asymmetrical loading during wedge splitting testing to investigate the mechanical properties of refractory materials. We also used digital image correlation technique to investigate the crack propagations of refractory materials under asymmetrical loading. The influence of asymmetrical wedge angle on the fracture parameters determination and crack propagation of refractories has been studied and compared to the results with symmetric loading.

2.2 Materials and experimental methods

2.2.1 Materials

In order to investigate the influence of microstructure and brittleness on the crack propagation behaviors of refractories, two typical refractory materials were selected: pure magnesia (M) and magnesia spinel (MA) materials. The chemical compositions and several physical properties of these two materials are shown in Table 1.

Table 1: Chemical composition and selected properties of pure magnesia (M) and magnesia spinel (MA) materials

	MgO	Al_2O_3	Fe_2O_3	CaO	SiO_2	Density (g/cm^3)	Apparent Porosity (%)	CCS (MPa)
M	97.0%	0.1%	0.2%	1.9%	0.6%	3.02	15	55
MA	87.9%	10.5%	0.5%	0.8%	0.3%	2.95	16	65

There are some micro-cracks around the spinel inclusions which is caused by the thermal expansion mismatch existing between magnesia matrix (α_{MgO}=13.3·10^{-6} K^{-1}) and spinel inclusions ($\alpha_{MgAl2O4}$=8.9·10^{-6} K^{-1}). These microcrack formations take place

during the cooling stage of the firing process [46]. Furthermore, to the existence of microcracks also contributes to the lower Young´s Modulus and density of magnesia spinel material.

2.2.2 Dimensions of specimens

Normally, the specimen size used in WST is 100 mm×100 mm×75 mm. However, limited by the original geometry of bricks, the specimen size of magnesia spinel specimen was 100 mm×100 mm×71 mm and the size of pure magnesia was 100 mm×100 mm×65 mm in this study. The notch length a was 27mm. The schematic representation of specimen geometry is illustrated in Fig.18, where w is the width of the groove and it changes with respect to the wedge angle (shown in Table 2); y is the distance between initial contact point and the gravity center of ligament; h is the ligament height.
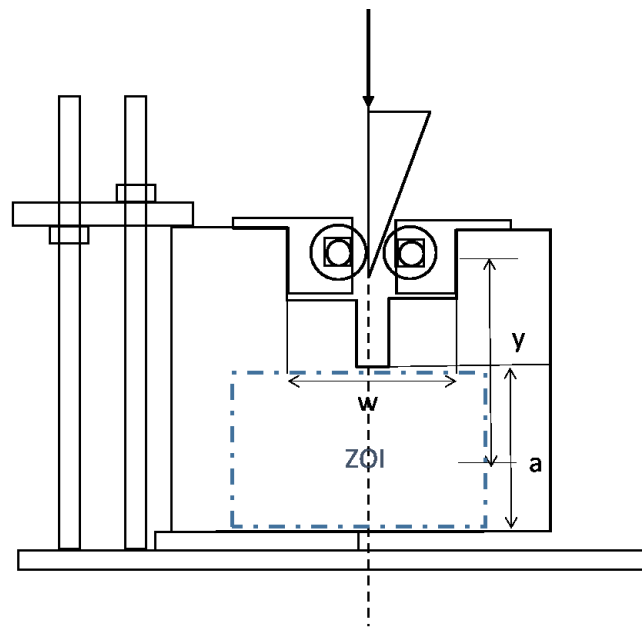
Fig.18: Schematic representation of wedge splitting test

Table 2: specimen width of different wedge angles

Angle (°)	5.2	10	15	20	22.5	30	35	10(Sym)
w(mm)	40.5	41	42	42.5	43	44	45	41

2.2.3 Experimental methods (WST and DIC)

As described above, the wedge splitting test (WST) has already been frequently applied to study the fracture behavior of brittle or quasi-brittle materials. The normal procedure of WST is applying the symmetric loads on specimens. In this research, we used asymmetrical wedge angle 5.2°, 10°, 15°, 20°, 22.5°, 30° and 35°during the wedge splitting test，and compared the results to those of the case with symmetrical wedge angle 10°. In the case of the asymmetrical loading condition, a device to fix the specimen during the test was demanded (shown in Fig.19a). In the meanwhile, two rollers were situated in the groove of the specimen and the wedge was inserted between two rollers.
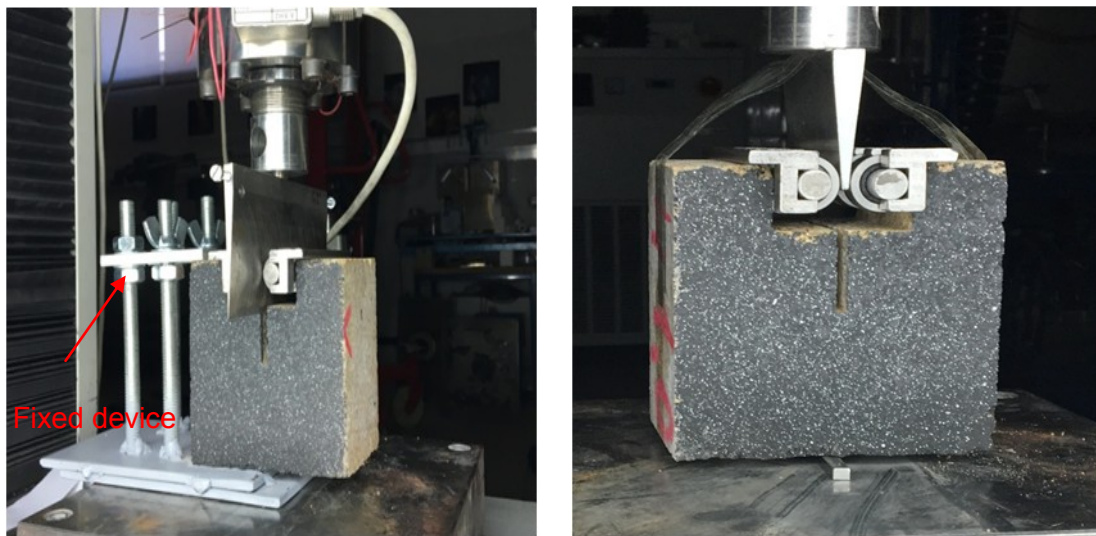
Fig.19: a) Asymmetrical loading device and b) Symmetrical loading device

The vertical force (F_V) is measured by a load cell. The horizontal force (F_H) is calculated from F_V using Eq. (21):

$$F_H = \frac{F_V}{tan\,(\beta)} \tag{21}$$

where β is the asymmetrical wedge angle. For symmetric loading, the Eq. (15) was applied.

The WST was carried out with a loading velocity of 0.5 mm/min, and load and displacement were measured in the vertical condition. After test, a load-displacement curve was generated, and the fracture mechanical parameters of refractories can be determined from these data.

The specific fracture energy G_F is determined by integrating the area under the load-displacement curve divided by the projected fracture area A during stable crack propagation, as shown in Eq. (16). In this research δ is the vertical displacement at 20% of the maximum load. The nominal notch tensile strength σ_{NT} can be calculated from the maximum horizontal load $F_{H,\max}$ using Eq. (17).

In addition to the experimental setup, a CMOS digital camera with a resolution of 5184×3456 pixels[2] was used to record the images during the wedge splitting test (illustrated in Fig.20). It is placed in front of the speckled surface to perform optical measurements by digital image correlation technique. This allows studying crack propagation during wedge splitting tests and the strain state around the crack tip. The acquisition frequency was 1 image every 2 seconds. The scale factor of the camera is 0.03 mm/pixel. After gaining the images we used the MatchID (DIC-2D software) to analyze the experimental results. In order to increase the contrast and obtain a random distribution of gray level on the specimen surface, we sprayed white spots on a black opaque layer.

Fig.20: The camera used to record images

The correlation process of DIC was performed on the zone of interest (ZOI). The zone of interest (ZOI), on which the calculation was done, is represented in Fig.19. The correlation algorithm located a subset in the reference image and searched the same subset in the images of the deformed sample. The step size was the distance between the center points of two consecutive subsets. Then the strain field is calculated from the displacement field based on the strain window algorithm [22]. The DIC parameters, including the subset size, step size and strain window size, are important for image correlation performance. The influences of these parameters were

shown in many investigations [47-49]. In this study, we chose a step size of 8 pixels, a subset size of 32×32 pixels^2 and a strain window size of 15×15 pixel^2.

2.3 Mechanical results

2.3.1 Mechanical properties under symmetrical loading condition

Fig.21 shows the vertical load–vertical displacement curves of magnesia spinel and pure magnesia materials obtained by wedge splitting test under symmetrical loading condition with the wedge angle of 10°. Three specimens were used for the measurement. The magnesia spinel material (Fig.21a) showed a significant post-peak region that was characterized by a mild descending curve with a mean ultimate vertical displacement of piston longer than 5 mm at 20% residual force. A sharp decrease of vertical load after peak load was observed for the pure magnesia material. The mean ultimate vertical displacement of piston was less than 4 mm at 20% residual force. Besides, the magnesia spinel material showed more consistent load/displacement curves, while the pure magnesia material presented higher scatter curves.
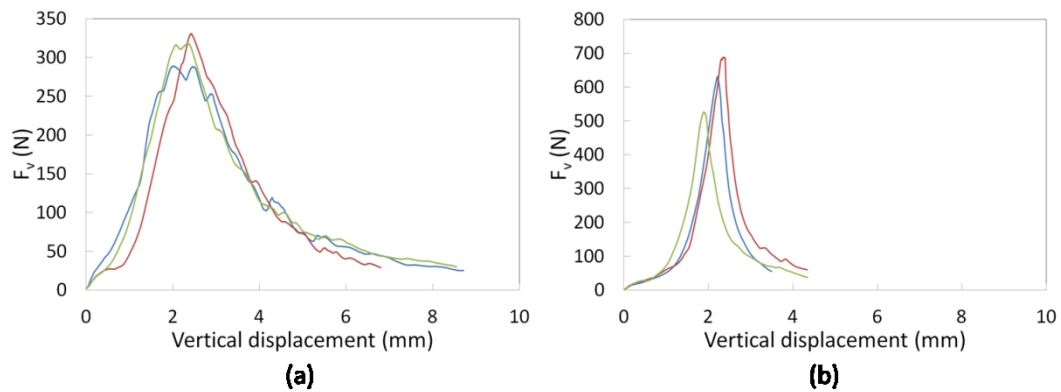
Fig.21: Vertical load-displacement curves of a) magnesia spinel and b) pure magnesia obtained by WST

Table 3 shows the average value of maximum vertical force $F_{v,max}$, maximum horizontal force $F_{H,max}$, nominal notch tensile strength σ_{NT} ,specific fracture energy G_F and the ratio of G_F/σ_{NT} for both materials. The fracture energy was calculated till 20% of the maximum vertical force reached in the descending curve. Although the pure magnesia material had higher tensile strength, its specific fracture energy was less than that of magnesia spinel material. The ratio G_F/σ_{NT} is a parameter to indicate the brittleness of the material: the more brittle material is, the lower value of the ratio is.

Magnesia spinel material has higher ratio than the pure magnesia material [43]. The pre-existing microcracks caused by mismatch of CTE contribute to brittleness reduction.

Table 3: Results of the mechanical properties

	$F_{v,max}$(N)	$F_{H,max}$(N)	σ_{NT}(MPa)	G_F(N/m)	G_F/σ_{NT}(μm)
M	614.9	3513.9	9.4	166.6	17.7
MA	312.7	1786.7	4.5	224.3	49.8

2.3.2 Mechanical properties under asymmetrical loading condition

The vertical force-displacement curves of all the different asymmetrical wedge angles are shown in the Fig.22-28. From all the diagrams, we can see that after reaching to the maximum vertical force, the vertical force decline of magnesia spinel material was relatively mild. On the contrary, the vertical force decline of pure magnesia material was sharp. Particularly from the asymmetrical wedge angle 20° to 35°, it dropped to 20% residual force immediately. Comparing with the figures of these two materials in the same asymmetrical wedge angle, the vertical displacement of magnesia spinel material was higher than that of pure magnesia material. For both materials, with the increasing of the asymmetrical wedge angles, the vertical displacement decreases. In addition, the post-peak load/displacement curves of magnesia spinel material were more stable than the curves of the pure magnesia material under asymmetrical loading. Especially at the asymmetrical wedge angle of 15°, 20° and 22.5°, the curves of pure magnesia material were particularly unstable.

(a)   (b)
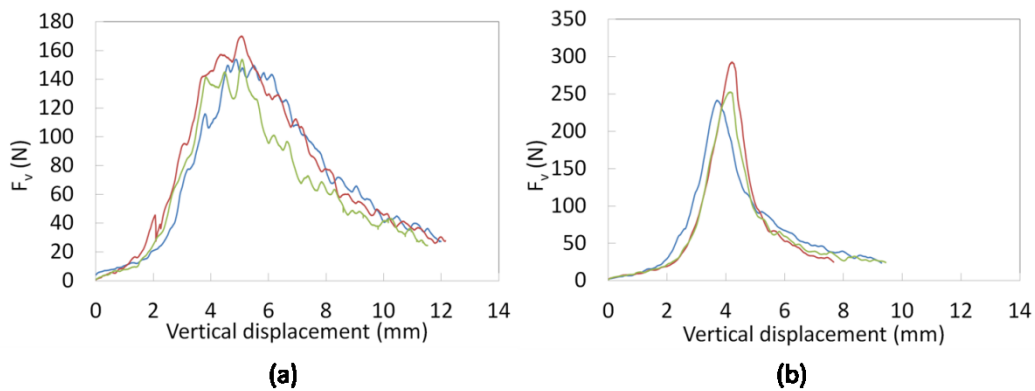
Fig.22: Vertical load-displacement curves obtained under asymmetrical wedge angle 5.2° of a) the magnesia spinel material and b) the pure magnesia material

(a)   (b)
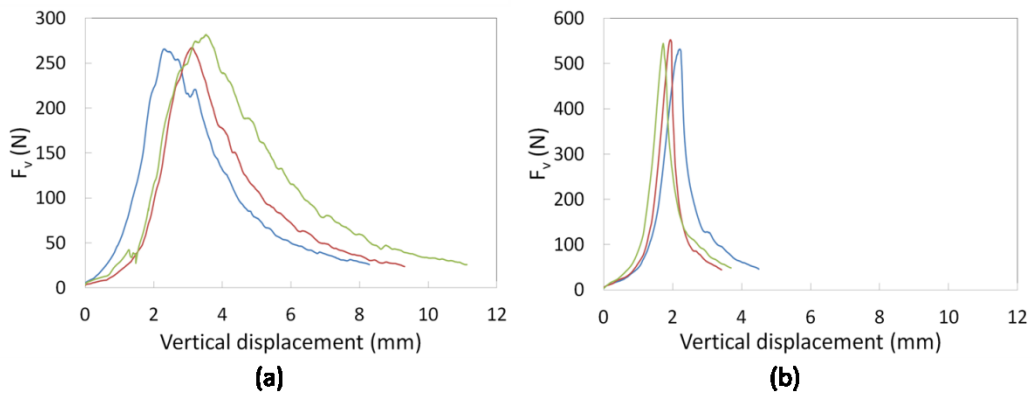
Fig.23: Vertical load-displacement curves obtained under asymmetrical wedge angle 10° of a) the magnesia spinel material and b) the pure magnesia material

(a)   (b)
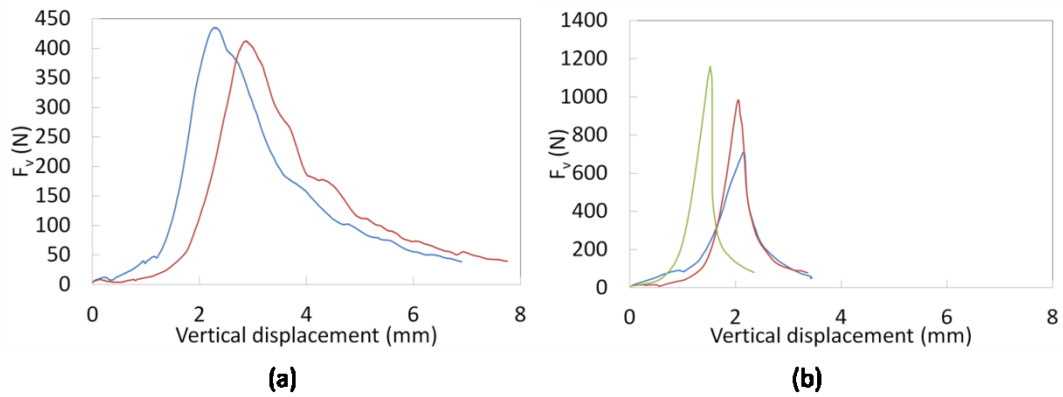
Fig.24: Vertical load-displacement curves obtained under asymmetrical wedge angle 15° of a) the magnesia spinel material and b) the pure magnesia material

(a)   (b)
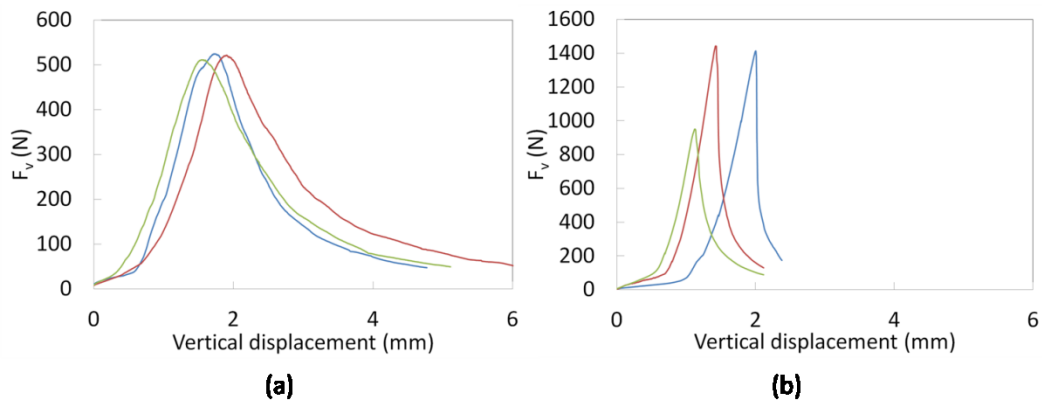
Fig.25: Vertical load-displacement curves obtained under asymmetrical wedge angle 20° of a) the magnesia spinel material and b) the pure magnesia material
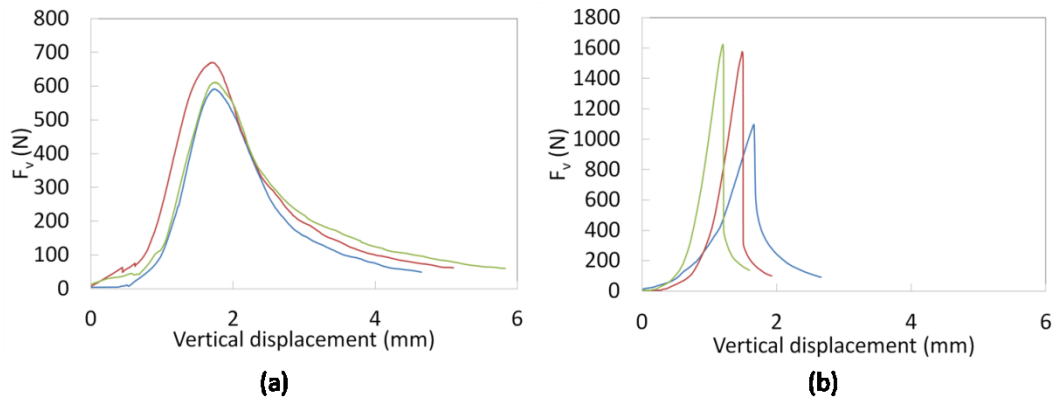
Fig.26: Vertical load-displacement curves obtained under asymmetrical wedge angle 22.5° of a) the magnesia spinel material and b) the pure magnesia material
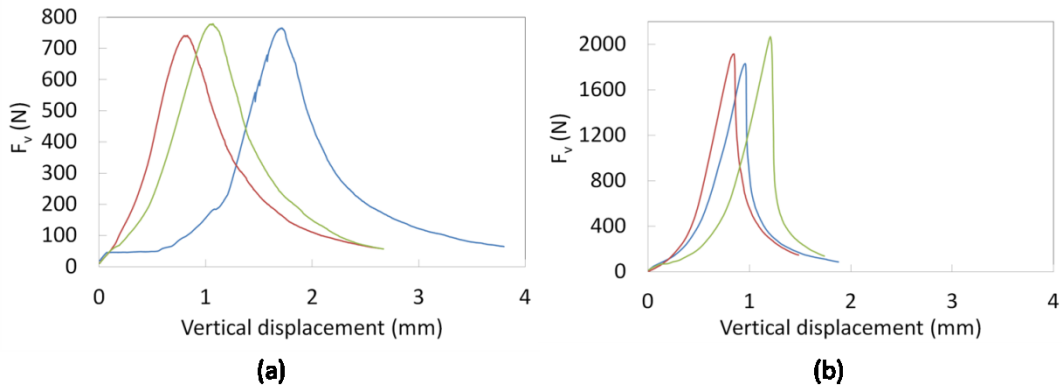
Fig.27: Vertical load-displacement curves obtained under asymmetrical wedge angle 30° of a) the magnesia spinel material and b) the pure magnesia material
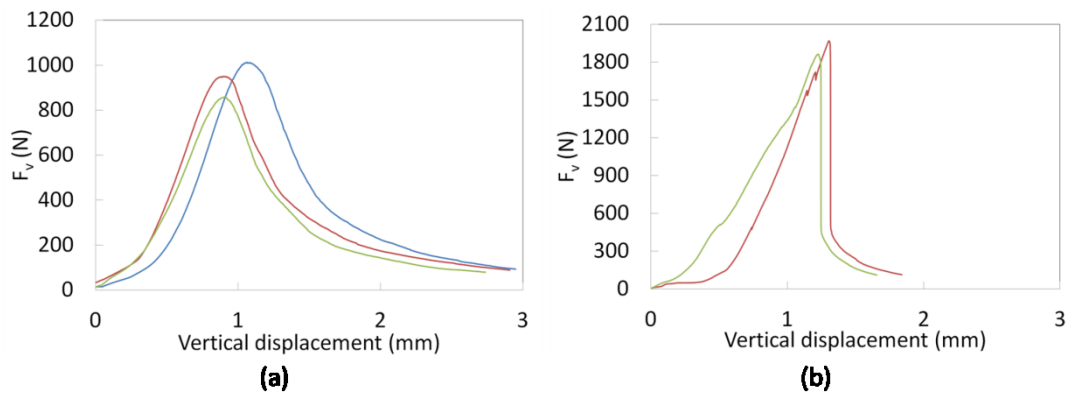
Fig.28: Vertical load-displacement curves obtained under asymmetrical wedge angle 35° of a) the magnesia spinel material and b) the pure magnesia material

The average values of vertical displacement at the moment of 20% residual force for different asymmetrical wedge angles are shown in Fig.29. It is obvious that the vertical displacement at the moment of 20% residual force decreased with increasing asymmetrical wedge angles in both materials. From the wedge angle 5.2° to 10°, it decreased very fast, and afterwards the reduction of vertical displacement at the moment of 20% residual force slowed down. Besides, the vertical displacement of magnesia spinel material was higher than that of pure magnesia material.
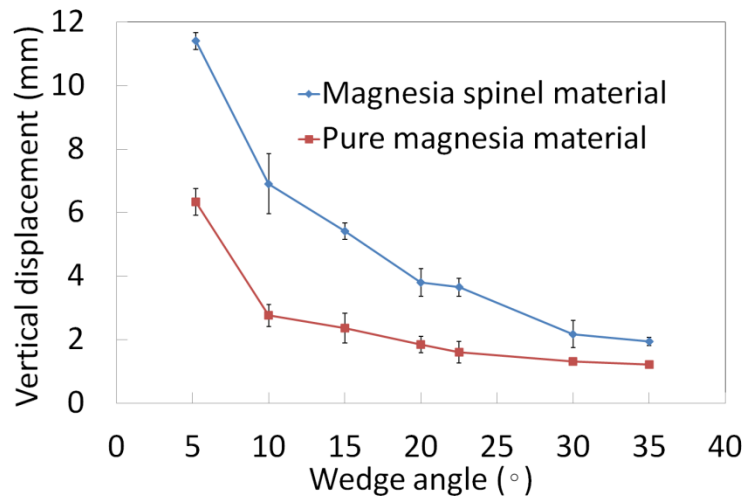
Fig.29: Average values of vertical displacement at the moment of 20% residual force of both materials under asymmetrical loading

Fig.30 illustrates the average values of maximum vertical force of magnesia spinel and pure magnesia materials under different asymmetrical and symmetrical wedge angles obtained by wedge splitting test. With increasing wedge angle, the maximum vertical force was increased for both materials. The maximum vertical forces of magnesia spinel materials (Fig.30a) were lower in comparison with those of pure magnesia materials (Fig.30b). Compared to the symmetrical loading, the cases with asymmetrical wedge angle of 10°showed slightly lower maximum vertical forces.
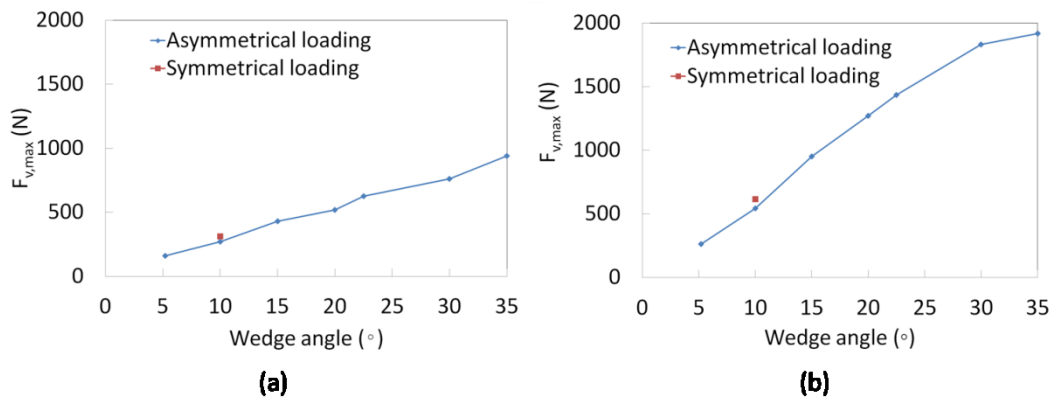
Fig.30: Maximum vertical forces of a) magnesia spinel and b) pure magnesia under different asymmetrical and symmetrical wedge angles

Fig.31 presents the average value of specific fracture energy G_F under different asymmetrical and symmetrical wedge angles for magnesia spinel and pure magnesia materials. The fracture energy was calculated till 20% of the maximum vertical force reached in the descending curve. The specific fracture energy of the magnesia spinel material did not show monotonous tendency with increasing asymmetrical wedge. The maximum specific fracture energy occurred when the wedge of 22.5° was applied. In contrast, the specific fracture energy of the pure magnesia material showed proportional relation to the asymmetrical wedge angle. That is to say, the specific fracture energy increased with increasing asymmetrical wedge angle. From the Fig.31, it is obvious that the fracture energy of magnesia spinel material under asymmetrical loading condition was higher than the pure magnesia materials. Compared to the symmetrical loading condition with 10° wedge angle, the specific fracture energies under asymmetrical angle 10° condition were slightly lower in both materials.
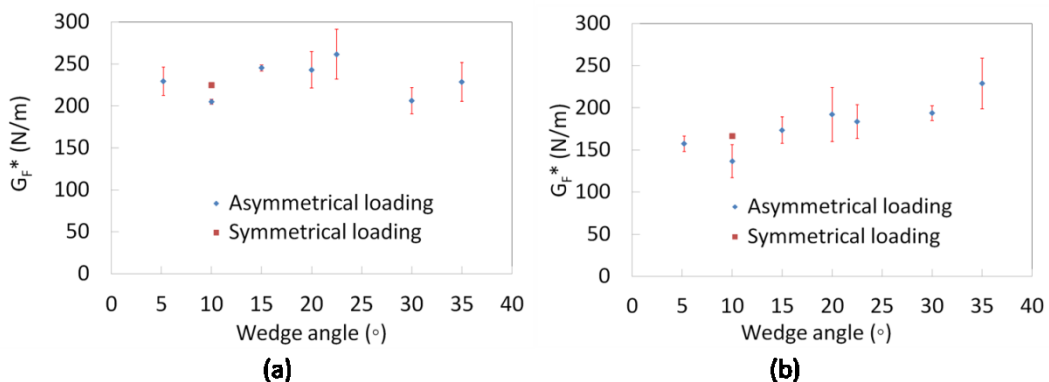
Fig.31: Specific fracture energy of a) magnesia spinel and b) pure magnesia under different asymmetrical and symmetrical wedge angles

The results of nominal notch tensile strength σ_{NT} under different asymmetrical wedge angles of these two materials are shown in Fig.32. In the case of the magnesia spinel material, the nominal notch tensile strength decreased with respect to the asymmetrical wedge angle. In contrast, the nominal notch tensile strength of the pure magnesia material increased with the asymmetrical wedge angle and reached a plateau in 15-22.5°. Afterwards, evident drop of the nominal notch tensile strength was observed. Generally, the notch tensile strength of the pure magnesia material was higher than that of the magnesia spinel material tested under the same asymmetrical wedge angle. Moreover, the standard deviation of the data of pure magnesia was higher than magnesia spinel material.
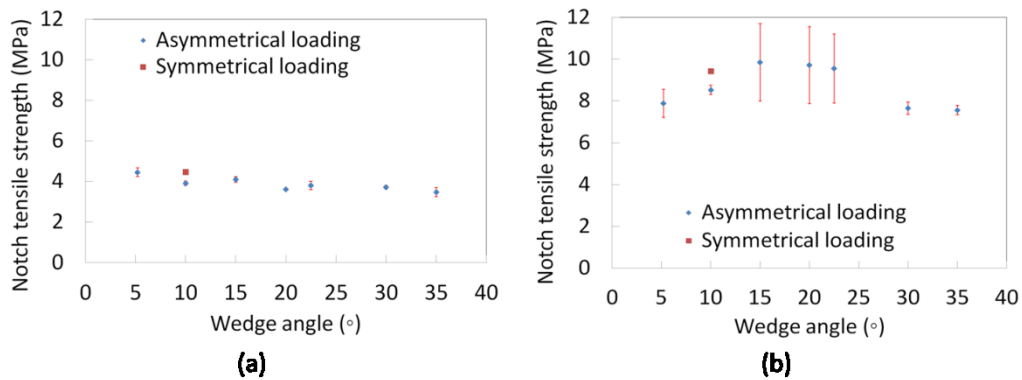
Fig.32: Nominal notch tensile strength of a) magnesia spinel and b) pure magnesia under different asymmetrical and symmetrical wedge angles

2.4 DIC results

2.4.1 Crack propagation behavior under symmetrical loading condition

Based on digital image correlation technique, the evolution of the strains along X-axis (perpendicular to the loading direction) is presented for different instances corresponding to different loading states (shown in Fig.33 and Fig.34). These images correspond to the zone of interest (ZOI) defined in Fig.18. According to the crack propagation of these two materials, we chose five images of different loading stages in Fig. 33a and four images in Fig.33b.
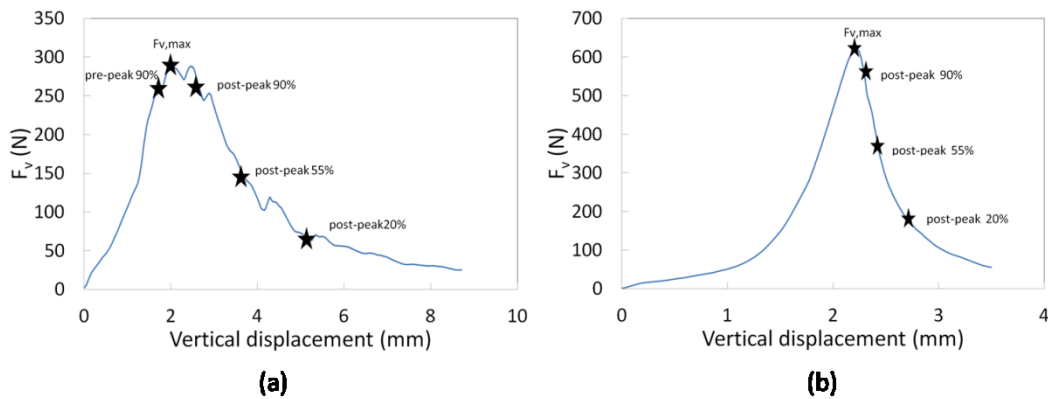
Fig.33: Vertical forces vs. displacement curve of a) magnesia spinel material and b) pure magnesia material

To underline the crack branching phenomenon, a specific strain color scale was chosen, in order to identify the evolution of local strains and to eliminate measurement noises. The strain below the threshold is marked grey. According to Fig.34, the initiation and the propagation of the crack of magnesia spinel material take place before reaching maximum load ($F_{v,max}$). A damaged zone in the neighborhood of the crack tip developed. This zone became wider and extended with the increase of the applied load. Branching of microcracks can be seen evidently during load descending. It is due to the pre-existing micro-cracks in magnesia spinel material. To the contrary, because of less pre-existing micro-cracks in pure magnesia material, the crack propagation behavior of pure magnesia was totally different. There was no crack branching phenomenon, only the main macro-crack can be observed. Moreover, before reaching the maximum force ($F_{v,max}$), almost no crack can be observed. From this figure, at 90% of the maximum force, the crack length in the spinel material looks like higher than pure magnesia material.
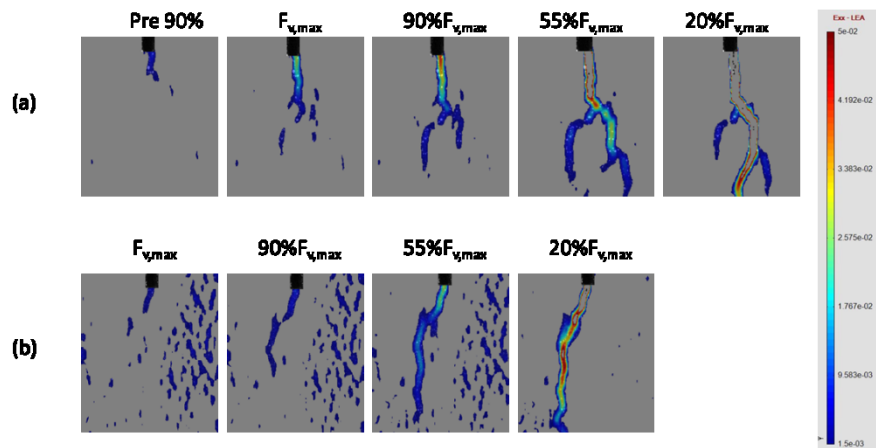
Fig.34: Images of X-axis of a) magnesia spinel material and b) pure magnesia material

2.4.2 Crack propagation behavior under asymmetrical loading condition

Fig.35 shows the process of crack propagation of magnesia spinel material under different asymmetrical wedge angles. The strain of all these images gained from digital image correlation is along X-axis which is perpendicular to the loading direction. From the Fig.35, the macro-crack of magnesia spinel developed prior to the maximum load and extended further with the loading. All of specimens showed a crack branching behavior after reaching the critical force during the wedge splitting test. As the extension of the macro-crack, the branches evolved from micro-cracks decreased which leads to a reduction of the fracture process zone. When the fracture process zone tip reached the bottom of the specimen, the crack propagation slowed down. In the cases of asymmetrical wedge angle 30° and 35°, the macro-crack before the critical force was almost invisible and after reaching the critical force it grew fast. Furthermore, comparing Fig.35b with the Fig.34a, branches in the case of asymmetrical loading was less than the case of symmetrical loading.
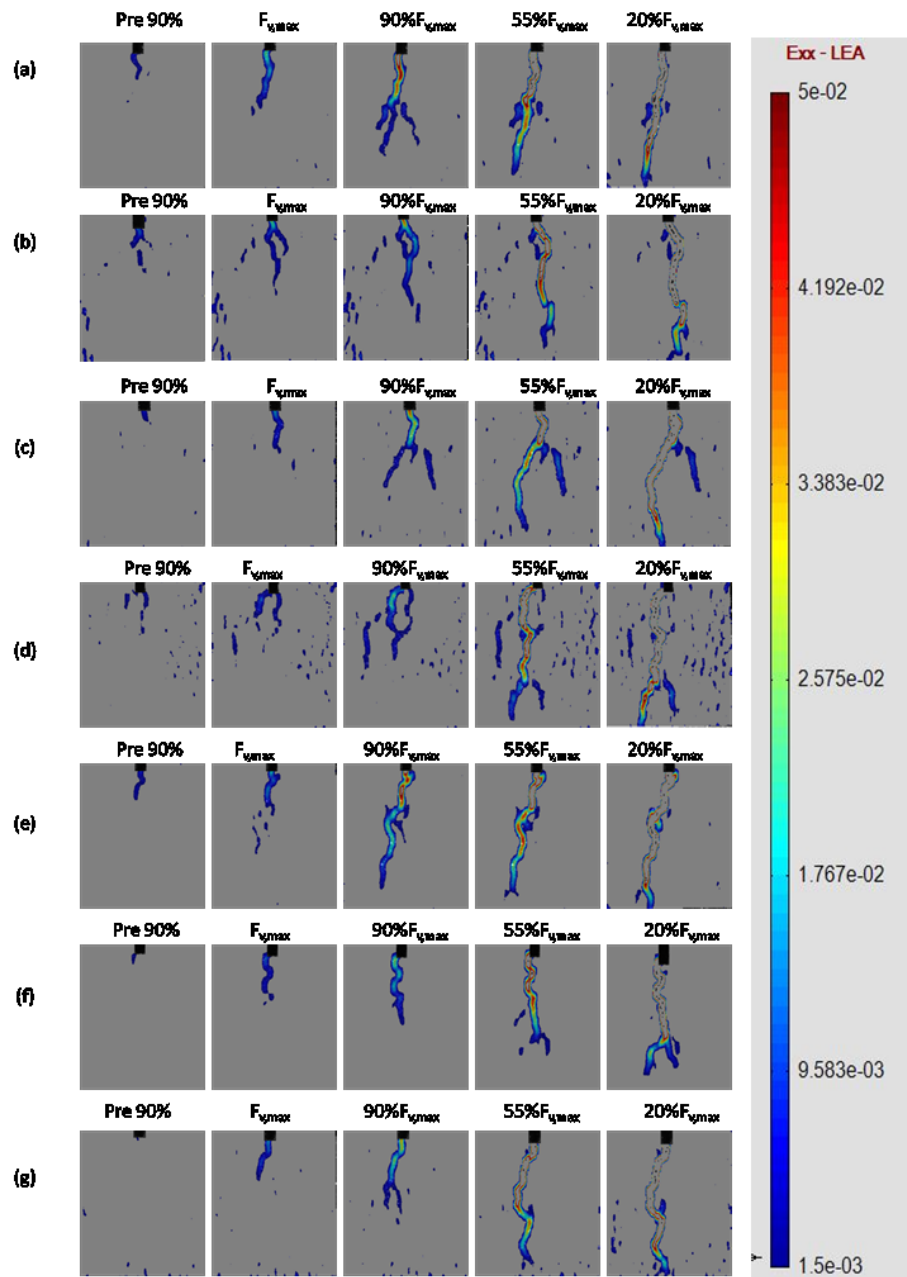
Fig.35: Images of X-axis of magnesia spinel material under asymmetrical wedge angle (a)5.2°, (b)10°, (c) 15°, (d) 20°, (e)22.5°, (f)30°and (g)35°

Fig.36 presents the process of crack propagation in the pure magnesia material under different asymmetrical wedge angles. From the asymmetrical wedge angle 20° to 35° only three images are shown. This is because the vertical force decrease too fast and the macro-crack in the pure magnesia material is formed instantly. It proves that with increasing the asymmetrical wedge angle, the crack propagates faster.
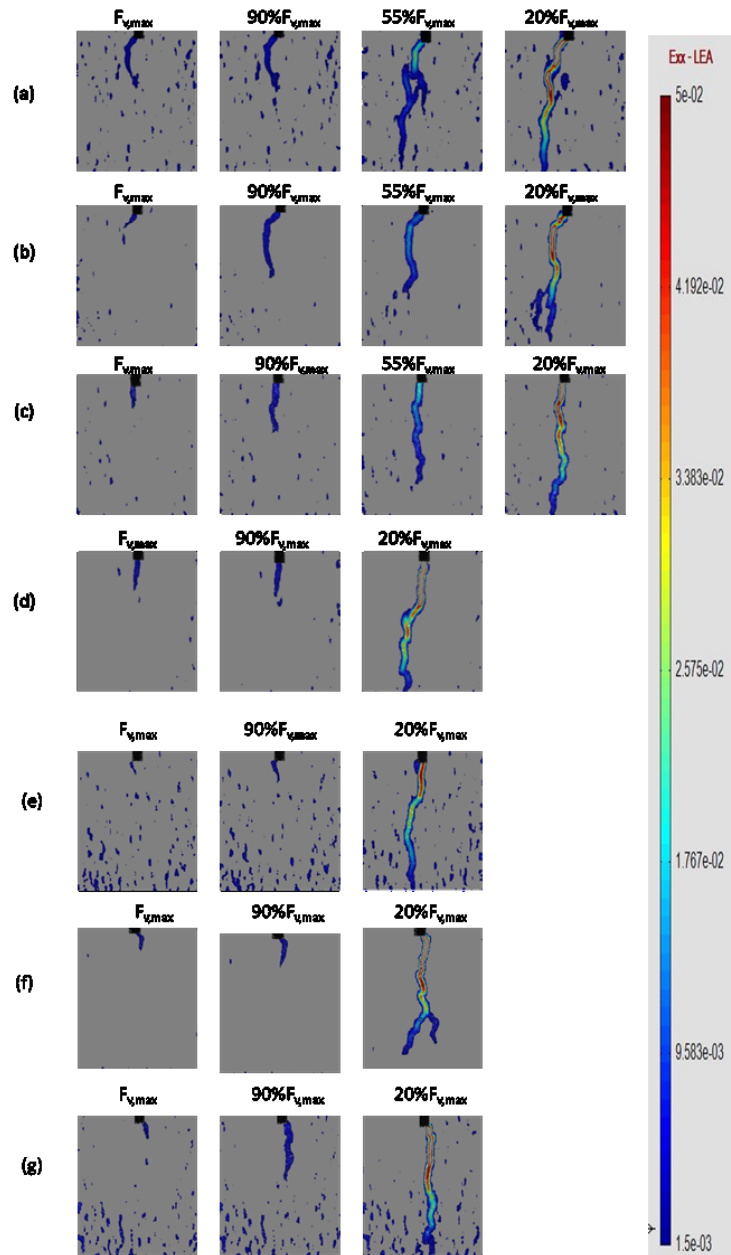
Fig.36: Images of X-axis of pure magnesia material under asymmetrical wedge angle (a)5.2°, (b)10°, (c) 15°, (d) 20°, (e)22.5°, (f)30°and (g)35°

2.4.3 Investigation of main crack propagation

In the process zone ahead of the macro-crack, energy dissipation processes take place. In order to investigate the main crack propagation, we chose several events to measure the main crack length (L_m), as shown in Fig.37a. The software which I used to measure the crack length was Image J and evaluation procedure is presented in Fig. 37b.

(a) (b)
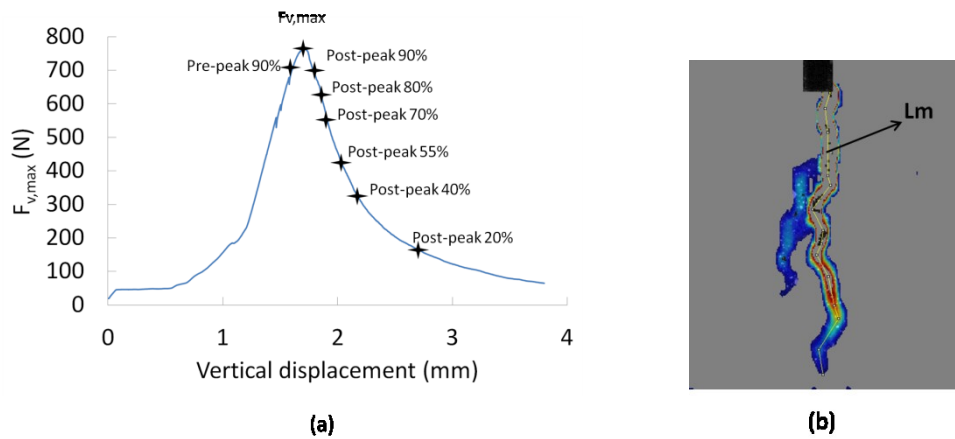
Fig.37: a) The specific points in the load-displacement curve and b) representation of crack length evaluation

Fig.38 shows the different fracture behavior for magnesia spinel and pure magnesia material. L is the main crack length at a certain force of the load-displacement curve, $L_{pre\ 90\%}$ is the main crack length when ascending force is 90% of maximum vertical force, $L_{Fv,max}$ is the main crack length at maximum vertical force, h is the ligament height of the specimen and $F_{v,pos}$ is the vertical force during force descending. The relative main crack length is defined as the ratio of the difference between the L_m and the $L_{pre\ 90\%}$ and the ligament height h. The magnesia spinel material exhibited a higher relative main crack length compared to the pure magnesia material when $F_{v,pos}/F_{v,max}$ is 1.0. The difference between the main crack lengths L_m of these two materials indicates the different development of the fracture process zone. The fracture process zone of magnesia spinel material developed prior to reaching the maximum load and increased with the loading, but the main crack of pure magnesia material occurred nearly at the load peak.   For both materials, the final relative crack lengths under asymmetrical loading were higher than that under symmetrical loading.
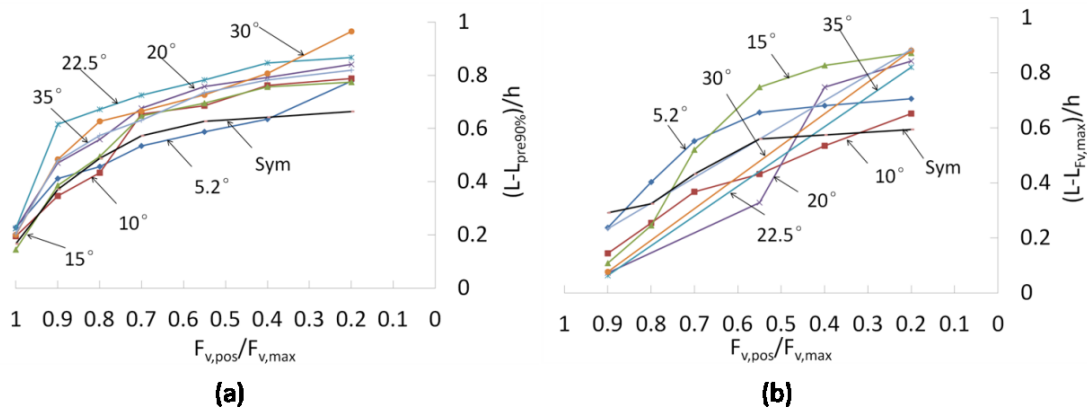
Fig.38: a) Relative main crack length of magnesia spinel material (and b) pure magnesia material with respect to load descending

Fig.39 illustrated the fracture process zone of these two materials at the moment of maximum load under the asymmetrical wedge angle 10°. In the case of magnesia spinel material, a significant fracture process zone was developed compared to the specimen size, but the pure magnesia material showed a very small fracture process zone. Besides, in comparison with the Fig.34 and Fig.39 it is obvious that the size of fracture process zone of symmetrical loading at the moment of maximum load was bigger than the case of asymmetrical loading in both materials.
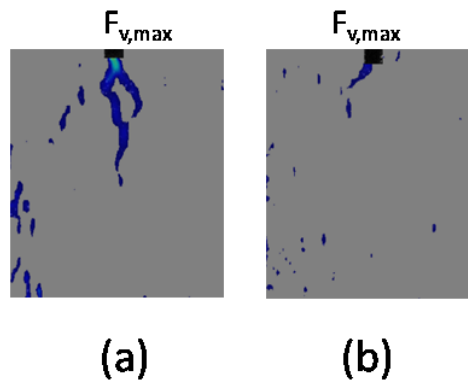
Fig.39: The process zone for a) the magnesia spinel material and b) the pure magnesia material at the moment of maximum vertical force under asymmetrical loading wedge angle 10°

2.5 Conclusions

The fracture behavior of two typical industrially produced refractory materials (magnesia spinel and pure magnesia materials) was investigated in this study. The difference in the mechanical behavior of these two materials is caused by microstructural differences. The microstructure characterized by pre-existing micro-cracks increases the thermal shock resistance and decrease the brittleness of magnesia spinel material.

In order to study the influence of wedge angles during asymmetrical loading on the fracture parameters, wedge splitting test associated with digital image correlation was used in this work. By calculation of the fracture parameters (the nominal notch tensile strength and the specific fracture energy) and DIC analysis the influences of different wedge angles were clarified. The specific fracture energy of the magnesia spinel material does not show monotonous tendency with increasing asymmetrical wedge. The nominal notch tensile strength decreases with respect to asymmetrical wedge angle. In contrast, the specific fracture energy of pure magnesia increases with increasing asymmetrical wedge angle. The notch tensile strength of the pure magnesia material increases with the asymmetrical wedge angle and reaches a plateau in 15-22.5°. Moreover, the notch tensile strength and fracture energy under asymmetrical loading is lower than in the case of symmetrical loading.

The fracture behavior of refractory materials is characterized by the development of the fracture process zone and the macro-crack. In the case of magnesia spinel material, the fracture process zone develops prior to the maximum load and is larger. With the extension of the macro-crack, crack branching decreases. Under symmetrical loading, more crack branches can be observed than the case of asymmetrical loading. For the pure magnesia material, crack propagation occurs immediately after reaching the maximum vertical load and the fracture process zone is very small. During the crack propagation process no crack branching can be observed. Furthermore, for both materials, the macro crack propagation is more instable with increasing asymmetrical wedge angles.

References

[1] Tschegg, E.K., Stanzl-Tschegg, S. E. (1999). Austrian Patent, AT 409038.

[2] Tschegg, E. K. (1986). Testing device and appropriate specimen shapes for tests to measure fracture values. Austrian Patent, AT 390328.

[3] Harmuth, H., & Tschegg, E. K. (1994). Fracture mechanical characterisation of ordinary ceramic refractory materials. Veitsch-Radex Rundsch. (1), 465-480.

[4] Griffith, A. A. (1921). The phenomena of rupture and flow in solids. Philosophical Transactions of the Royal Society of London. Series A, containing papers of a mathematical or physical character, 221, 163-198.

[5] Irwin, G. R. (1997). Analysis of stresses and strains near the end of a crack traversing a plate. SPIE Milestone series MS, 137(167-170), 16.

[6] Sakai, M. (1988). Fracture mechanics of refractory materials. Taikabutsu Overseas, 8(2), 4-12.

[7] Rice, J. R. (1968). A path independent integral and the approximate analysis of strain concentration by notches and cracks. Journal of Applied Mechanics, 35(2), 379-386.

[8] Hübner, H., & Jillek, W. (1977). Sub-critical crack extension and crack resistance in polycrystalline alumina. Journal of Materials Science, 12(1), 117-125.

[9] Evans, A. G., & Faber, K. T. (1984). Crack-growth resistance of microcracking brittle materials. Journal of the American Ceramic Society, 67(4), 255-260.

[10] Sakai, M., & Bradt, R. C. (1986). Graphical methods for determining the nonlinear fracture parameters of silica and graphite refractory composites. In Fracture Mechanics of Ceramics (pp. 127-142). Springer US.

[11] Green, D. J., Hawkins, C. A., & Hirlinger, M. M. (1983). Double cantilever beam testing of a transversely isotropic fibrous silica material. Journal of the American Ceramic Society, 66(1), 46-49.

[12] Bradt, R. C. (1981). Problems and possibilities with cracks in ceramics. In Proc. 11th International Conf. on Science of Ceramics held at Stenungsund, Sweden, June 14-17, 1981. Edited by R. Carlsson and S. Karlsson. Swedish Ceram. Soc., Gothenburg, Sweden, 1981. (p. 349).

[13] Dugdale, D. S. (1960). Yielding of steel sheets containing slits. Journal of the Mechanics and Physics of Solids, 8(2), 100-104.

[14] Barenblatt, G. I. (1959). The formation of equilibrium cracks during brittle

fracture. Journal of Applied Mathematics and Mechanics, 23(3), 622-636.

[15] Hillerborg, A., Modéer, M., & Petersson, P. E. (1976). Analysis of crack formation and crack growth in concrete by means of fracture mechanics and finite elements. Cement and Concrete Research, 6(6), 773-781.

[16] Hillerborg, A. (1991). Application of the fictitious crack model to different types of materials. International Journal of Fracture, 51(2), 95-102.

[17] Hasselman, D. P. H. (1963). Elastic energy at fracture and surface energy as design criteria for thermal shock. Journal of the American Ceramic Society, 46(11), 535-540.

[18] Hasselman, D. P. H. (1969). Unified theory of thermal shock fracture initiation and crack propagation in brittle ceramics. Journal of the American Ceramic Society, 52(11), 600-604.

[19] Nakayama, J. (1965). Direct measurement of fracture energies of brittle heterogeneous materials. Journal of the American Ceramic Society, 48(11), 583-587.

[20] Tattersall, H. G., & Tappin, G. (1966). The work of fracture and its measurement in metals, ceramics and other materials. Journal of Materials Science, 1(3), 296-301.

[21] Brühwiler, E., & Wittmann, F. H. (1990). The wedge splitting test, a new method of performing stable fracture mechanics tests. Engineering Fracture Mechanics, 35(1-3), 117-125.

[22] Lava, P., Cooreman, S., & Debruyne, D. (2010). Study of systematic errors in strain fields obtained via DIC using heterogeneous deformation generated by plastic FEA. Optics and Lasers in Engineering, 48(4), 457-468.

[23] Linsbauer, H. N., & Tschegg, E. K. (1986). Fracture energy determination of concrete with cube-shaped specimens. Zement und Beton, 31, 38-40.

[24] Löfgren, I. (2004). The wedge splitting test a test method for assessment of fracture parameters of FRC. In Fracture Mechanics of Concrete Structures, Vol 2. Proceedings of the Fifth International Conference on Fracture Mechanics of Concrete and Concrete Structures. In Vail, Colorado/USA/12-16 April 2004 (Vol. 2, pp. 1155-1162).

[25] Stanzl-Tschegg, S. E., Tan, D. M., & Tschegg, E. K. (1995). New splitting method for wood fracture characterization. Wood Science and Technology, 29(1), 31-50.

[26] Tschegg, E.K. (1991).New equipments for fracture tests on concrete. Materialprüfung, 33(11/12), 338-342.

[27] Harmuth, H. (1995). Stability of crack propagation associated with fracture energy determined by wedge splitting specimen. Theoretical and Applied Fracture

Mechanics, 23(1), 103-108.

[28] Jin, S.L. (2015). Investigation of compressive refractory creep. Doctoral thesis, Chair of Ceramics, Montanuniversität Leoben.

[29] McGinnis, M., & Pessiki, S. (2006). Experimental and numerical development of the core-drilling method for the nondestructive evaluation of in-situ stresses in concrete structures. Doctoral thesis, Civil and Environmental Engineering Department, Lehigh University.

[30] Bruck, P., Esselman, T., & Fallin, M. (2012). Digital image correlation for nuclear. Nuclear Engineering International, 57(693), 28-31.

[31] Schmidt, T., Tyson, J., Revilock, D. M., Padula, S., Pereira, J. M., Melis, M., & Lyle, K. (2005). Performance verification of 3D image correlation using digital high-speed cameras. In Proceedings of the 2005 SEM Annual Conference and Exposition, Portland, Oregon.

[32] Barranger, Y., Doumalin, P., Dupré, J. C., & Germaneau, A. (2012). Strain measurement by digital image correlation: influence of two types of speckle patterns made from rigid or deformable marks. Strain, 48(5), 357-365.

[33] Lin, Q., & Labuz, J. F. (2011). Identifying quasi-brittle fracture by AE and digital imaging. Journal of Acoustic Emission, 29, 68-77.

[34] Chen, D. J., Chiang, F. P., Tan, Y. S., & Don, H. S. (1993). Digital speckle-displacement measurement using a complex spectrum method. Applied Optics, 32(11), 1839-1849.

[35] Robert, L., Nazaret, F., Cutard, T., & Orteu, J. J. (2007). Use of 3-D digital image correlation to characterize the mechanical behavior of a fiber reinforced refractory castable. Experimental Mechanics, 47(6), 761-773.

[36] Schmitt, N., Berthaud, Y., & Poirier, J. (2000). Tensile behavior of magnesia carbon refractories. Journal of the European Ceramic Society, 20(12), 2239-2248.

[37] Marzagui, H., Cutard, T., Yeugo Fogain, E., Huger, M., Gault, C., Prompt, N., & Deteuf, C. (2004). Microstructural changes and high temperature mechanical behavior of an andalusite based low cement refractory castable. Proceedings of Advances in Refractories for the Metallurgical Industries IV (COM'2004), Hamilton, Canada, 331-345.

[38] Nazaret, F., Marzagui, H., & Cutard, T. (2006). Influence of the mechanical behaviour specificities of damaged refractory castables on the Young's modulus determination. Journal of the European Ceramic Society, 26(8), 1429-1438.

[39] Nazaret, F., Cutard, T., & Bernhart, G. (2004). Thermomechanical behavior of a

fiber reinforced refractory concrete: tests and FE analysis. Proceedings of the 6th RILEM Symposium on Fiber Reinforced Concrete (BEFIB 2004), Varenna, Lake Como, Italy (pp. 689-698).

[40] Vic-2Dr and Vic-3Dr softwares (2006) Correlated Solutions Incorporated, http://www.correlatedsolutions.com/.

[41] Orteu, J. J., Cutard, T., Garcia, D., Cailleux, E., & Robert, L. (2007). Application of stereovision to the mechanical characterization of ceramic refractories reinforced with metallic fibers. Strain, 43(2), 96-108.

[42] Routschka, G. (1997). Refractory Materials. Essen: Vulkan-Verlag, ISBN 3-8027-3147-6.

[43] Lemaistre, H. (1998). Etude des propriétés thermomécaniques de divers réfractaires. Doctoral dissertation, National Institute of Applied Sciences of Lyon.

[44] Belrhiti, Y., Pop, O., Germaneau, A., Doumalin, P., Dupré, J. C., Harmuth, H., & Chotard, T. (2015). Investigation of the impact of micro-cracks on fracture behavior of magnesia products using wedge splitting test and digital image correlation. Journal of the European Ceramic Society, 35(2), 823-829.

[45] Andreev, K., Sinnema, S., Rekik, A., Allaoui, S., Blond, E., & Gasser, A. (2012). Compressive behaviour of dry joints in refractory ceramic masonry. Construction and Building Materials, 34, 402-408.

[46] Fasching, C., Gruber, D., & Harmuth, H. (2015). Simulation of micro-crack formation in a magnesia spinel refractory during the production process. Journal of the European Ceramic Society, 35(16), 4593-4601.

[47] Wang, Y., Lava, P., Coppieters, S., De Strycker, M., Van Houtte, P., & Debruyne, D. (2012). Investigation of the uncertainty of DIC under heterogeneous strain states with numerical tests. Strain, 48(6), 453-462.

[48] Yaofeng, S., & Pang, J. H. (2007). Study of optimal subset size in digital image correlation of speckle pattern images. Optics and Lasers in Engineering, 45(9), 967-974.

[49] Bornert, M., Brémand, F., Doumalin, P., Dupré, J. C., Fazzini, M., Grédiac, M. & Robert, L. (2009). Assessment of digital image correlation measurement errors: methodology and results. Experimental Mechanics, 49(3), 353-370.